

© 2025 IEEE. Personal use of this material is permitted. Permission from IEEE must be obtained for all other uses, including reprinting/republishing this material for advertising or promotional purposes, collecting new collected works for resale or redistribution to servers or lists, or reuse of any copyrighted component of this work in other works. This work has been submitted to the IEEE for possible publication. Copyright may be transferred without notice, after which this version may no longer be accessible.

All-Electric Heavy-Duty Robotic Manipulator: Actuator Configuration Optimization and Sensorless Control

Mohammad Bahari, Amir Hossein Barjini, Pauli Mustalahti, and Jouni Mattila

Abstract—This paper presents a unified framework that integrates modeling, optimization, and sensorless control of an all-electric heavy-duty robotic manipulator (HDRM) driven by electromechanical linear actuators (EMLAs). An EMLA model is formulated to capture motor electromechanics and direction-dependent transmission efficiencies, while a mathematical model of the HDRM, incorporating both kinematics and dynamics, is established to generate joint-space motion profiles for prescribed TCP trajectories. A safety-ensured trajectory generator, tailored to this model, maps Cartesian goals to joint space while enforcing joint-limit and velocity margins. Based on the resulting force and velocity demands, a multi-objective Non-dominated Sorting Genetic Algorithm II (NSGA-II) is employed to select the optimal EMLA configuration. To accelerate this optimization, a deep neural network, trained with EMLA parameters, is embedded in the optimization process to predict steady-state actuator efficiency from trajectory profiles. For the chosen EMLA design, a physics-informed Kriging surrogate, anchored to the analytic model and refined with experimental data, learns residuals of EMLA outputs to support force and velocity sensorless control. The actuator model is further embedded in a hierarchical virtual decomposition control (VDC) framework that outputs voltage commands. Experimental validation on a one-degree-of-freedom EMLA testbed confirms accurate trajectory tracking and effective sensorless control under varying loads.

Index Terms—All-electric heavy-duty robotic manipulators; electromechanical linear actuators (EMLAs); multi-objective optimization; physics-informed Kriging (PIK); virtual decomposition control (VDC).

I. INTRODUCTION

The escalating urgency of the climate crisis, underscored by the Paris Agreement [1] and the European Union’s 2035 ban on internal-combustion vehicles [2], is accelerating the decarbonization of off-highway machinery and mobile working machines [3], [4]. Within this category, heavy-duty robotic manipulators (HDRMs) have traditionally relied on hydraulic linear actuators (HLAs) for their high power density in heavy-payload tasks [5]. However, the multiple energy conversion stages from electrical generation to hydraulic pressure to mechanical motion introduce significant inefficiencies, with actuator efficiencies often below 50% due to leakage, throttling losses, and auxiliary cooling demands [6], [7]. Performance further degrades with fluid compressibility and viscosity variations, which impair response speed and positional accuracy under changing loads and temperatures [8].

Funding for this research was provided by the Business Finland partnership project “Future All-Electric Rough Terrain Autonomous Mobile Manipulators” (Grant No. 2334/31/2022) and the Research Council of Finland under the Project “Nonlinear PDE-model-based control of flexible manipulators” (Grant No. 355664).

All authors are with the Faculty of Engineering and Natural Sciences, Tampere University, 33720 Tampere, Finland. Corresponding author: Mohammad Bahari (mohammad.bahari@tuni.fi).

In addition, frequent maintenance such as leak inspections, filter replacement, and oil top-ups increases downtime and costs, while spilled hydraulic fluid creates environmental and cleanup risks.

Amid these challenges, and as cities mandate carbon-free public works by 2025 [9], attention is shifting toward electromechanical linear actuators (EMLAs) [10]. Powered by permanent magnet synchronous motors (PMSMs) and precision screw transmissions, EMLAs eliminate fluid-based losses, enable regenerative braking during load-lowering cycles [11], and support integrated, high-bandwidth sensing essential for stability-guaranteed control. Furthermore, PMSM-driven EMLAs benefit from low-cogging-torque designs for ultra-smooth motion [12] and provide accurate feedback for high-precision, fault-tolerant position sensing [13], [14].

From a control perspective, a wide range of strategies have been investigated for HDRMs, including genetic neural networks [15], nonlinear model predictive control [16], data-driven reinforcement learning [17], adaptive neural network control [18], backstepping-based schemes [19], and virtual decomposition control (VDC) [20]. In parallel, numerous controllers have been proposed for PMSMs [21], [22]. However, the strong coupling between low-level actuator dynamics and high-level manipulator behavior underscores the need to analyze and design the control system as an integrated whole [23]. Within this context, modular frameworks such as VDC are particularly well-suited for evaluating and coordinating the performance of EMLAs in HDRMs [23]. Moreover, conventional PMSM torque and speed control requires multiple measurements that may be unavailable or impractical in many experimental setups [24]. Reducing dependence on such measurements through sensorless strategies therefore improves practicality by eliminating costly or failure-prone sensors.

Electrifying HDRMs with EMLAs and enabling robust, sensorless control requires a cohesive, end-to-end framework: one that captures EMLA dynamics and manipulator kinematics/dynamics, supports actuator configuration decisions for given trajectory demands, and ensures reliable control through sensorless strategies. To this end, the main contributions of this paper are summarized as follows:

- 1) An EMLA model is obtained that integrates PMSM dynamics with direction-dependent screw-transmission efficiency, and is embedded through VDC into the HDRM joint-space kinematics and dynamics that are derived in this work.
- 2) A safety-ensured trajectory generator is designed, tailored to the HDRM model, to map Cartesian trajectories into joint space and enforce joint limits and velocity

margins to guarantee feasible motion execution under varying payloads.

- 3) An EMLA configuration framework is formulated as a multi-objective NSGA-II problem over the motor, gear-box ratio, and screw lead, accelerated by a deep neural network model that delivers fast efficiency predictions of the actuator.
- 4) A physics-informed Kriging (PIK) model is developed for the optimized EMLA to enable sensorless control with precise estimation of load-side force and velocity using only torque and angular velocity measurements, and integrated within the VDC framework. The unified controller is experimentally validated on a one-DOF EMLA testbed, demonstrating accurate trajectory tracking under varying loads.

II. DYNAMIC MODELING OF THE EMLA

EMLAs provide precise motion conversion and high efficiency in all-electric HDRMs, which requires a unified model of PMSM electromechanics and screw-drive transmission losses. This section derives the PMSM voltage and torque equations, formulates the screw-drive kinematics with directional friction efficiency, and integrates both into a complete actuator dynamic model.

A. PMSM Equations

Let $\mathbf{i}_{abc} = [i_a, i_b, i_c]^T$ and $\mathbf{v}_{abc} = [v_a, v_b, v_c]^T$ denote the phase currents and phase voltages, respectively. The stator resistance matrix is defined as $\mathbf{R}_s = \text{diag}(r_a, r_b, r_c)$, with inductance matrix \mathbf{L}_s , and the flux-linkage vector Ψ_{abc} . Here, P is the pole-pair count, ψ_f is the permanent-magnet flux linkage per pole, and the flux linkage vector can be written as $\Psi_{abc} = \psi_f \frac{d}{dt} [\cos \theta_\gamma(t), \cos \theta_\delta(t), \cos \theta_\zeta(t)]^T$. In compact form, the stator phase voltage of PMSM is expressed as (1).

$$\mathbf{v}_{abc} = \mathbf{R}_s \mathbf{i}_{abc} + \frac{d}{dt} (\mathbf{L}_s \mathbf{i}_{abc}) + \Psi_{abc}. \quad (1)$$

The Park transformation maps the stationary-frame vector $\mathbf{s}_{abc} = [s_a, s_b, s_c]^T$ into the rotating $dq0$ frame as $\mathbf{s}_{dq0} = \mathbf{T}_p \mathbf{s}_{abc}$, where $\mathbf{s}_{dq0} = [s_d, s_q, s_0]^T$, as detailed in [25]. Accordingly, the voltage equations in the $dq0$ frame are expressed as (2).

$$\mathbf{v}_{dq0} = \mathbf{T}_p \mathbf{R}_s \mathbf{T}_p^{-1} \mathbf{i}_{dq0} + \mathbf{T}_p \frac{d}{dt} (\mathbf{L}_s \mathbf{T}_p^{-1} \mathbf{i}_{dq0}) + \mathbf{T}_p \mathbf{T}_p^{-1} \Psi_{dq0}. \quad (2)$$

Assuming a balanced three-phase PMSM with equal stator resistances, the current dynamics and the electromagnetic torque are expressed as (3) [26].

$$\begin{cases} \frac{di_d}{dt} = \frac{1}{L_d} v_d - \frac{r_s}{L_d} i_d + \frac{L_q}{L_d} P \omega_m i_q, \\ \frac{di_q}{dt} = \frac{1}{L_q} v_q - \frac{r_s}{L_q} i_q - \frac{L_d}{L_q} P \omega_m i_d - \frac{P \psi_f \omega_m}{L_q}, \\ \tau_e = 1.5P [\psi_f i_q + (L_d - L_q) i_d i_q]. \end{cases} \quad (3)$$

Remark 1: The PMSM phase voltages are generated by a voltage-source inverter (VSI) using pulse-width modulation

(PWM). The actuator controller first computes the required dq -axis voltages (v_d, v_q), which are converted to three-phase duty cycles via the inverse Park transform. The PWM module then modulates these duty cycles to produce the switching signals S_1 – S_6 , which yield the phase voltages \mathbf{v}_{abc} applied to the motor.

B. Transmission Mechanism and Dynamic Model

An EMLA's screw drive converts motor rotary motion into linear displacement via the ratio $n = 2\pi/\rho$, where ρ is the screw lead. Thread friction results in direction-dependent efficiencies: η_f is forward efficiency when the motor overcomes friction and load, and η_b is backdriving efficiency when loads back-drive the screw. Defining the lead angle $\phi = \arctan(\rho/(2\pi r_m))$ and friction angle $\lambda = \arctan(\mu)$, the screw efficiency η_s is given by:

$$\eta_s^\pm = \begin{cases} \eta_f = \frac{\tan(\phi(\rho))}{\tan(\phi(\rho) + \lambda(\mu))}, & \dot{x}_L \geq 0, \\ \eta_b = \frac{\tan(\phi(\rho) - \lambda(\mu))}{\tan(\phi(\rho))}, & \dot{x}_L < 0. \end{cases} \quad (4)$$

Denoting gearbox efficiency by η_g , the direction-aware transmission efficiency model η_t^\pm in terms of gear ratio N_g , μ , and ρ is expressed as $\eta_t^\pm = \eta_g(N_g) \times \eta_s^\pm(\mu, \rho)$. Accounting for Coulomb friction τ_c , viscous damping f_v , and external load F_L , the EMLA dynamics are given in (5)–(6):

$$\begin{cases} \ddot{x}_L = \frac{nN_g(\tau_e - \tau_c - \kappa_f(f_v \dot{x}_L + F_L))}{M_t + nN_g \kappa_f J_m}, \\ \text{where } \ddot{x}_L \geq 0 \text{ and } \kappa_f = nN_g \eta_t^+. \end{cases} \quad (5)$$

$$\begin{cases} \ddot{x}_L = \frac{\kappa_b(\tau_e - \tau_c - nN_g f_v \dot{x}_L) - F_L}{M_t + nN_g \kappa_b J_m}, \\ \text{where } \ddot{x}_L < 0 \text{ and } \kappa_b = \frac{nN_g \eta_g}{\eta_b}. \end{cases} \quad (6)$$

where M_t and J_m denote the total moving mass and the motor inertia, respectively.

III. MATHEMATICAL MODELING OF THE MANIPULATOR AND SAFETY-ENSURED TRAJECTORY GENERATION

Building on the EMLA model presented in Section II, we integrate manipulator and actuator dynamics via the VDC framework [27] to derive the kinematic and dynamic equations, and then introduce a safety-guaranteed trajectory planner that enforces each EMLA's allowable operating range.

A. Kinematic and Dynamic Equations of the Manipulator

Remark 2: The detailed kinematic and dynamic equations are derived in Algorithms 5 and 6. In the rest of this section, we only summarize the key preliminaries of the VDC approach.

Definition 1: Let $\{\mathbf{A}\}$ be a three-dimensional orthogonal coordinate system attached to a rigid body. The origin's linear velocity in frame $\{\mathbf{A}\}$ is denoted by ${}^A\mathbf{v} \in \mathbb{R}^3$, and its angular velocity by ${}^A\boldsymbol{\omega} \in \mathbb{R}^3$. These are combined into the six-dimensional linear/angular velocity vector ${}^A\mathbf{V} =$

$[{}^A\mathbf{v}^T, {}^A\boldsymbol{\omega}^T]^T \in \mathbb{R}^6$, commonly used in rigid body dynamics to represent translational and rotational motion in a unified form [27].

Now consider another frame $\{\mathbf{B}\}$, also attached to the same rigid body. The linear/angular velocity vector transforms between frames $\{\mathbf{A}\}$ and $\{\mathbf{B}\}$ as:

$${}^B\mathbf{V} = {}^A\mathbf{U}_B^T {}^A\mathbf{V}, \quad (7)$$

where ${}^A\mathbf{U}_B \in \mathbb{R}^{6 \times 6}$ is the spatial velocity transformation matrix defined as:

$${}^A\mathbf{U}_B = \begin{bmatrix} {}^A\mathbf{R}_B & \mathbf{0}_{3 \times 3} \\ ({}^A\mathbf{r}_{AB} \times) {}^A\mathbf{R}_B & {}^A\mathbf{R}_B \end{bmatrix}, \quad (8)$$

with ${}^A\mathbf{R}_B \in \mathbb{R}^{3 \times 3}$ denoting the rotation matrix from frame $\{\mathbf{B}\}$ to $\{\mathbf{A}\}$, and ${}^A\mathbf{r}_{AB} = [r_x, r_y, r_z]^T$ the position vector from $\{\mathbf{A}\}$ to $\{\mathbf{B}\}$, expressed in $\{\mathbf{A}\}$. The associated skew-symmetric cross-product operator is:

$$({}^A\mathbf{r}_{AB} \times) = \begin{bmatrix} 0 & -r_z & r_y \\ r_z & 0 & -r_x \\ -r_y & r_x & 0 \end{bmatrix}. \quad (9)$$

In the VDC framework, the vector $\mathbf{V} \in \mathbb{R}^6$ is sequentially transformed from the base to the end-effector, ensuring consistent motion representation throughout the kinematic chain.

Definition 2: Let ${}^A\mathbf{f} \in \mathbb{R}^3$ and ${}^A\boldsymbol{\tau} \in \mathbb{R}^3$ denote the force and moment vectors applied to a rigid body, both expressed in frame $\{\mathbf{A}\}$. The combined force/moment vector is given by ${}^A\mathbf{F} = [{}^A\mathbf{f}^T, {}^A\boldsymbol{\tau}^T]^T \in \mathbb{R}^6$. In the VDC framework, this vector is propagated from the end-effector to the base [27].

Now, consider another frame $\{\mathbf{B}\}$ attached to the same body. The force/moment vector transforms between $\{\mathbf{A}\}$ and $\{\mathbf{B}\}$ as:

$${}^A\mathbf{F} = {}^A\mathbf{U}_B {}^B\mathbf{F}. \quad (10)$$

The net force/moment vector acting on the body, expressed in $\{\mathbf{A}\}$ and denoted by ${}^A\mathbf{F}^* \in \mathbb{R}^6$, is computed using:

$$\mathbf{M}_A \frac{d}{dt}({}^A\mathbf{V}) + \mathbf{C}_A {}^A\mathbf{V} + \mathbf{G}_A = {}^A\mathbf{F}^*, \quad (11)$$

where $\mathbf{M}_A \in \mathbb{R}^{6 \times 6}$ is the spatial mass matrix, $\mathbf{C}_A \in \mathbb{R}^{6 \times 6}$ represents Coriolis and centrifugal terms, and $\mathbf{G}_A \in \mathbb{R}^6$ is the gravity vector, all in frame $\{\mathbf{A}\}$. From (11), the dynamics can be expressed in regressor form:

$$Y_A \theta_A = \mathbf{M}_A \frac{d}{dt}({}^A\mathbf{V}) + \mathbf{C}_A {}^A\mathbf{V} + \mathbf{G}_A, \quad (12)$$

where $Y_A({}^A\dot{\mathbf{v}}, {}^A\mathbf{v}) \in \mathbb{R}^{6 \times 10}$ is the regressor matrix and $\theta_A(m, {}^A\mathbf{r}_{AB}, \mathbf{I}_A)$ the corresponding inertial parameter vector [28].

B. Safety-Ensured Trajectory Generation

To operate the all-electric HDRM, a trajectory generator computes the joint velocities required to reach a user-defined end-effector position in Cartesian space, using filtered joint angles as input, as shown in Fig. 7.

A fifth-order polynomial trajectory generator produces a smooth trajectory from the initial position $\mathbf{P}_{\text{start}}$ to the final position $\mathbf{P}_{\text{final}}$ over time t_{end} , yielding:

$$\begin{cases} \mathbf{P}_d(t) = [x_d, y_d, z_d]^T = \sum_{i=0}^5 \mathbf{a}_i t^i, \\ \dot{\mathbf{P}}_d(t) = [\dot{x}_d, \dot{y}_d, \dot{z}_d]^T = \sum_{i=1}^5 i \mathbf{a}_i t^{i-1}. \end{cases} \quad (13)$$

The coefficients $\mathbf{a}_i \in \mathbb{R}^3$ satisfy boundary conditions with zero initial/final velocities and accelerations. After $t > t_{\text{end}}$, the position is fixed at $\mathbf{P}_{\text{final}}$ and the velocity is set to zero.

Following the VDC method, the required end-effector velocity adds a correction term to the desired velocity:

$$\dot{\mathbf{P}}_r = \dot{\mathbf{P}}_d + \lambda(\mathbf{P}_d - \mathbf{P}), \quad (14)$$

where $\dot{\mathbf{P}}_r \in \mathbb{R}^3$ is the required velocity, \mathbf{P}_d and $\dot{\mathbf{P}}_d$ are the desired position and velocity, \mathbf{P} is the measured position, and λ is a positive gain.

The Cartesian-to-joint velocity mapping is derived using the Jacobian based on the Denavit–Hartenberg (DH) convention:

$$\dot{\mathbf{\Pi}} = \mathbf{J} \dot{\boldsymbol{\Theta}}, \quad (15)$$

where $\dot{\mathbf{\Pi}} \in \mathbb{R}^6$ is the end-effector velocity vector, $\mathbf{J} \in \mathbb{R}^{6 \times 6}$ is the Jacobian, and $\boldsymbol{\Theta}$ is the joint angle vector. Given $\dot{\mathbf{\Pi}}_r = [\dot{x}_r, \dot{y}_r, \dot{z}_r, 0, 0, 0]^T$, the required joint velocities are:

$$\dot{\boldsymbol{\Theta}}_r = \mathbf{J}^{-1} \dot{\mathbf{\Pi}}_r. \quad (16)$$

To enforce joint-level safety, a soft-limiting algorithm scales each required joint velocity $\dot{\zeta}_{i_r}$ as it nears its limit, resulting in:

$$\begin{cases} \dot{\zeta}_{i_r}^{\text{safe}} = s_i \cdot \dot{\zeta}_{i_r}, & \text{for } i = 1, \dots, 6, \\ s_i = \begin{cases} \frac{\zeta_i - \zeta_{\min,i}}{m_i}, & \text{if } \zeta_i \leq \zeta_{\min,i} + m_i \text{ and } \dot{\zeta}_{i_r} < 0, \\ \frac{\zeta_{\max,i} - \zeta_i}{m_i}, & \text{if } \zeta_i \geq \zeta_{\max,i} - m_i \text{ and } \dot{\zeta}_{i_r} > 0, \\ 1, & \text{otherwise,} \end{cases} \end{cases} \quad (17)$$

where $s_i \in [0, 1]$, $\zeta_{\min,i}$ and $\zeta_{\max,i}$ are joint limits, and m_i is the soft margin. This ensures smooth deceleration near limits, avoiding abrupt velocity changes.

IV. OPTIMIZATION FRAMEWORK

A. Problem Definition and Surrogate Training

The actuator-configuration optimization problem is formulated by selecting the PMSM, gearbox ratio, and screw lead that enable an EMLA to follow a prescribed HDRM joint-space force–velocity trajectory. The objectives are twofold: (i) maximize the steady-state efficiency of the EMLA, and (ii) minimize the nominal power rating of the PMSM. This yields a multi-objective problem solved using the Non-dominated Sorting Genetic Algorithm II (NSGA-II) [29]. NSGA-II is chosen for its ability to generate a diverse Pareto front without predefined weights and for its elitism mechanism, which preserves high-quality solutions across generations.

Each motor i in the catalog is characterized by a nominal shaft power P_{N_i} and a rated efficiency η_{N_i} . Let P_{req} denote

the mechanical power required at the load. A capable set of motors is defined by retaining only those indices i that satisfy $\eta_{N_i} \eta_t^\pm(N_g, \mu, \rho) P_{N_i} \geq P_{\text{req}}(F_{L_r}, \dot{x}_{L_r})$, so that $i \in \{1, \dots, n_c\}$ always corresponds to a PMSM capable of meeting the trajectory demands.

To reduce computational cost during optimization, rather than repeatedly invoking the full Simulink EMLA model, a deep neural network (DNN) model is trained. The DNN maps EMLA parameters and load-side motion profiles to the predicted steady-state efficiency, enabling rapid evaluations within the optimization loop. The resulting dataset is normalized and used to train a [64, 32, 16, 4]-layer feedforward network, with a 70/15/15 train/validation/test split. The trained network achieves a mean absolute error below 2%, reducing per-query evaluation time from tens of seconds to under one millisecond. The offline training procedure is summarized in Algorithm 1.

Algorithm 1 DNN Training for EMLA Efficiency

Require: PMSM parameters catalog $\{\text{motor}_i\}_{i=1}^M$
Require: Grids: load force F_L , linear velocities \dot{x}_L , gear ratios N_g , screw leads ρ , and i
Ensure: Trained DNN surrogate net and normalizers $x\text{Set}, y\text{Set}$

```

1:  $X \leftarrow \emptyset$  and  $Y \leftarrow \emptyset$ 
2: for  $i = 1$  to  $M$  do
3:   for all  $F \in F_L, v \in \dot{x}_L$  do
4:     for all  $G \in N_g, \ell \in \rho$  do
5:        $P_{\text{avail}} \leftarrow \eta_{N_i} \eta_t^\pm(N_g, \mu, \rho) \times P_{N_i}$ 
6:       if  $P_{\text{avail}} \leq F \cdot v$  then
7:         continue
8:       end if
9:       build params from  $\text{motor}_i, G, \ell$ 
10:       $\eta \leftarrow \text{SIMULINK}(\text{params}, F, v)$ 
11:      append  $[F, v, \text{params}]$  to  $X$ 
12:      append  $\eta$  to  $Y$ 
13:   end for
14: end for
15: end for
16:  $[X_n, x\text{Set}] \leftarrow \text{MAPMINMAX}(X)$ 
17:  $[Y_n, y\text{Set}] \leftarrow \text{MAPMINMAX}(Y)$ 
18:  $\text{net} \leftarrow \text{FITNET}([64, 32, 16, 4], \text{'trainlm'})$ 
19:  $\text{TRAIN}(\text{net}, X_n, Y_n)$ 
20:  $\text{SAVE}(\text{'EMLA\_DNN'}.mat, \text{net}, x\text{Set}, y\text{Set})$ 

```

Then, the manipulator's Cartesian trajectories are mapped into joint space using the VDC-derived HDRM kinematics and dynamics model (see Section III), yielding the required lift-joint force and linear velocity profiles, as shown in Fig. 1. These profiles (F_{L_r}, \dot{x}_{L_r}), together with the PMSM catalog, serve as inputs to the optimization. Algorithm 2 implements NSGA-II to solve the optimization problem in (18), where the efficiency term $\eta_{DNN}^{(i)}$ is predicted by the trained DNN model from Algorithm 1, evaluated for the i th motor. The constraints ensure that each candidate actuator configuration satisfies the required power and motion demands. Finally, the decision vector is defined as $\mathbf{x} = (i, N_g, \rho)$, where i is the motor

index. The optimization problem is therefore formulated as (18):

$$\begin{aligned}
\min_{\mathbf{x}=(i, N_g, \rho)} \quad & \mathbf{f}(\mathbf{x}) = \begin{pmatrix} -\eta_{DNN}^{(i)}(\text{params}, F_{L_r}, \dot{x}_{L_r}) \\ P_N^{(i)}(\tau_e, \omega_m) \end{pmatrix} \\
\text{s.t.} \quad & \eta_{DNN}^{(i)}(\text{params}, F_{L_r}, \dot{x}_{L_r}) P_N^{(i)}(\tau_e, \omega_m) \\
& \geq P_{\text{req}}(F_{L_r}, \dot{x}_{L_r}, \eta_s) \\
& i \in \{1, \dots, n_c\} \\
& N_{g,\min} \leq N_g \leq N_{g,\max} \\
& \rho_{\min} \leq \rho \leq \rho_{\max}
\end{aligned} \tag{18}$$

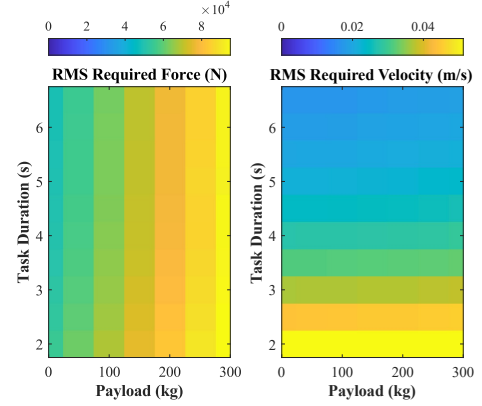


Fig. 1. Required lift-joint force (N) and velocity (m/s) as functions of payload and task duration. These profiles, derived from the HDRM model, define the force-velocity demands that serve as inputs to the optimization framework.

The optimization problem in (18) is solved using Algorithm 2, which outputs the Pareto front $\{(\eta_j, P_j)\}$ and the best actuator configuration (i^*, G^*, ℓ^*) .

B. EMLA Selection and Results

The optimization is executed across the operational envelope of the HDRM, spanning a wide range of payloads and task durations. From the resulting Pareto front, each payload-task duration pair is mapped to its corresponding optimized actuator configuration, defined by the selected motor index i^* , gearbox ratio G^* , and screw lead ℓ^* , as shown in Fig. 2.

The optimized designs exhibit clear trends in EMLA configuration across the operational envelope. For fast cycles, the NSGA-II selects the lowest gear-to-lead ratios, since excessive reduction or overly fine screw leads would unduly limit load-side speed. As cycle times lengthen, the required actuator speed decreases, so the algorithm increases the gear-to-lead ratio, trading top-end speed for mechanical advantage. This reduces the motor's power requirement and enables the selection of a smaller, lower-rated motor. Moreover, at any fixed cycle time, increasing payloads drive the optimal gear-to-lead ratio downward until the motor's nominal power becomes insufficient; at that point NSGA-II elevates to a higher-power motor rather than further changing the transmission parameters. Efficiency contours in Fig. 3 corroborate these

Algorithm 2 NSGA-II Optimization for EMLA Configuration

Require: Safety-ensured joint-space trajectory F_{L_r}, \dot{x}_{L_r}
Require: PMSM catalog $\{\text{motor}_i\}_{i=1}^M$
Require: Trained DNN model net with normalizers xSet, ySet from Algorithm 1

Ensure: Pareto front $\{(\eta_j, P_j)\}$ and best actuator configuration (i^*, G^*, ℓ^*)

- 1: Define decision vector $\mathbf{x} = (i, G, \ell)$
- 2: $i \in \{1, \dots, M\}, G \in [N_{g,\min}, N_{g,\max}], \ell \in [\rho_{\min}, \rho_{\max}]$
- 3: Compute required power $P_{\text{req}} \leftarrow F_{L_r} \dot{x}_{L_r}$
- 4: **function** OBJFUN($\mathbf{x}, F_{L_r}, \dot{x}_{L_r}$)
- 5: $\eta_{DNN} \leftarrow \text{EFFPRED}(\mathbf{x}, F_{L_r}, \dot{x}_{L_r}, \text{net}, \text{xSet}, \text{ySet})$
- 6: **return** $[-\eta_{DNN}, P_N^{(i)}]$
- 7: **end function**
- 8: **function** NONLCON(\mathbf{x})
- 9: $\tau_{\text{req}} \leftarrow F_{L_r} \ell (2\pi G \eta_t^\pm)^{-1}$
- 10: $n_{\text{req}} \leftarrow 60 G \dot{x}_{L_r} (\ell)^{-1}$
- 11: $\eta_{DNN} \leftarrow \text{EFFPRED}(\mathbf{x}, F_{L_r}, \dot{x}_{L_r}, \text{net}, \text{xSet}, \text{ySet})$
- 12: $c_1 \leftarrow P_{\text{req}} - \eta_{DNN} P_N^{(i)}$
- 13: $c_2 \leftarrow n_{\text{req}} - n_n^{(i)}$
- 14: $c_3 \leftarrow \tau_{\text{req}} - \tau_n^{(i)}$
- 15: **return** $[c_1, c_2, c_3]$
- 16: **end function**
- 17: Initialize population of decision vector (\mathbf{x})
- 18: $\{\text{Obj}, \text{Cons}\} \leftarrow \text{gamultiobj}(\text{ObjFun}, \text{NonlCon}, \dots)$
- 19: **for** each solution j **do**
- 20: $\eta_j \leftarrow -\text{Obj}(j, 1), P_j \leftarrow \text{Obj}(j, 2)$
- 21: Collect all non-dominated $\{(\eta_j, P_j)\}$
- 22: **end for**
- 23: Identify best configuration $\mathbf{x}_{j^*} = (i^*, G^*, \ell^*)$
- 24: **return** Pareto front $\{(\eta_j, P_j)\}$ and best configuration \mathbf{x}_{j^*}

design shifts, showing peak efficiency in the high-payload, fast-cycle regime and illustrating how larger motors at fast, heavy-load conditions, operating close to their nominal point can outperform lighter-load, slower-cycle configurations with smaller motors. This is a noteworthy result for the heavy-duty electrification industry, as it demonstrates that upsizing the motor can enhance overall actuation efficiency under the most demanding operating scenarios.

Overall, by integrating NSGA-II with the trained DNN for EMLA efficiency prediction, the framework systematically exploits the torque–speed landscape by jointly balancing motor power and actuator efficiency. This yields actuator configurations that are optimally matched to each payload–cycle requirement.

V. PHYSICS-INFORMED KRIGING SURROGATE FOR THE OPTIMIZED EMLA

This section develops a physics-informed Kriging (PIK) surrogate for the optimized EMLA configuration. Given the HDRM’s specific payload–duration requirements, NSGA-II first identifies the best actuator configuration, which then serves as the basis for constructing the PIK model. The surrogate integrates analytic motor physics into a Gaussian-

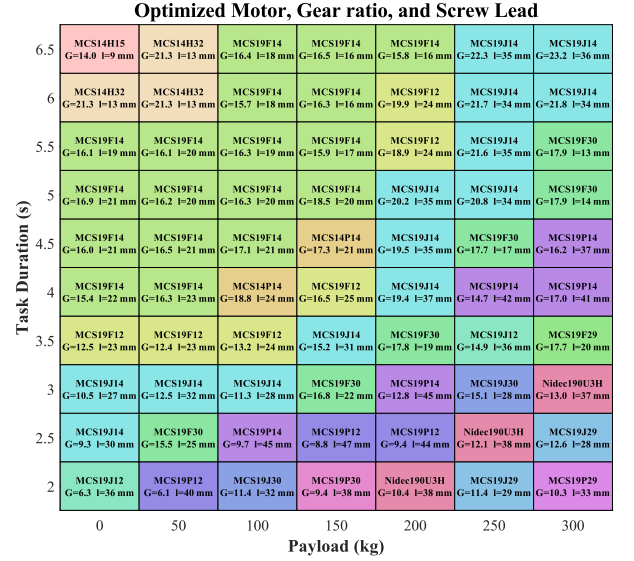


Fig. 2. Optimized EMLA configuration grid where each cell indicates the selected motor, gear ratio, and screw lead for the corresponding payload–task duration pair.

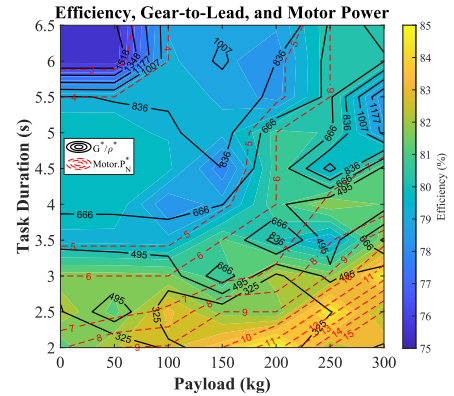


Fig. 3. Efficiency contour of the optimized EMLA configuration (%) with solid black isolines of gear-to-lead ratio and dashed red isolines of motor power (kW) as functions of payload and task duration.

process regression framework, enabling both high prediction accuracy and real-time computational efficiency.

Definition 3: In the Gaussian process regression framework, let $D \subseteq \mathbb{R}^d$ denote the input domain, with N observation locations $X = \{x^{(i)}\}_{i=1}^N$, where $x^{(i)} \in D$, and the associated scalar responses $y = (y^{(1)}, y^{(2)}, \dots, y^{(N)})^\top$, where $y^{(i)} \in \mathbb{R}$. The outputs are modeled as in (19), with the Gaussian process prior given in (20).

$$Y = (Y(x^{(1)}), Y(x^{(2)}), \dots, Y(x^{(N)}))^\top \quad (19)$$

$$Y(\cdot) \sim \mathcal{GP}(\mu(\cdot), k(\cdot, \cdot)), \quad (20)$$

where $\mu(x) = \mathbb{E}[Y(x)]$ and $k(x, x') = \text{Cov}\{Y(x), Y(x')\}$, while $x, x' \in D$. The prior covariance matrix $C \in \mathbb{R}^{N \times N}$ has entries $C_{ij} = k(x^{(i)}, x^{(j)})$, and define the noise-aware train-

ing covariance $K = C + \sigma_n^2 I$. The kernel hyperparameters are identified by maximizing the log-marginal likelihood

$$\begin{cases} \ln L = -\frac{1}{2} (y - \mu)^\top K^{-1} (y - \mu) - \frac{1}{2} \ln |K| - \frac{N}{2} \ln(2\pi), \\ \mu = (\mu(x^{(1)}), \dots, \mu(x^{(N)}))^\top. \end{cases} \quad (21)$$

For any test input $x^* \in D$, the predictive distribution takes the form

$$\begin{cases} Y(x^*) | X, y \sim \mathcal{N}(\hat{y}(x^*), \hat{s}^2(x^*)), \\ \hat{y}(x^*) = \mu(x^*) + c(x^*)^\top K^{-1} (y - \mu), \\ \hat{s}^2(x^*) = k(x^*, x^*) - c(x^*)^\top K^{-1} c(x^*), \end{cases} \quad (22)$$

where the cross-covariance vector is defined as

$$c(x^*) = (k(x^{(1)}, x^*), \dots, k(x^{(N)}, x^*))^\top. \quad (23)$$

Remark 3: Here we take $d = 2$, $D = \{(\tau_e, \omega_m)\} \subset \mathbb{R}^2$, and index inputs by $x^{(k)} = (\tau_e^k, \omega_m^k)$ for $k = 1, \dots, N$.

A. Experimental Testbed and Data Collection

The experimental setup employs an 11.6 kW, 8-pole Nidec190U3H PMSM (380/480 V) coupled with a gearbox and screw drive to form the EMLA, as shown in Fig. 4. The actuator's output is mechanically coupled to a secondary electrohydraulic cylinder that serves as a load emulator, generating dynamic, time-varying force profiles representative of HDRM lift-joint loading. Real-time signal acquisition and actuation feedback are handled via EtherCAT, ensuring precise synchronization and high-resolution monitoring.

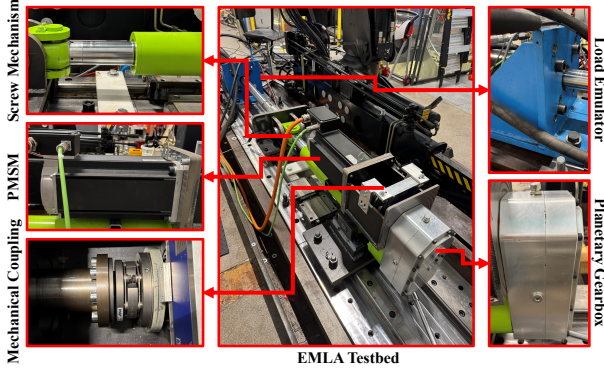


Fig. 4. Experimental EMLA testbed.

Load forces ranged over $F_L(t) \in [0, 70]$ kN, and linear velocities over $\dot{x}_L(t) \in [0, 0.07]$ m/s. All variables were sampled at 1 kHz. The raw time-series $\{\tilde{F}_L(t), \tilde{x}_L(t), \tilde{\eta}(t), \tilde{\tau}_e(t), \tilde{\omega}_m(t), \tilde{i}_{abc}(t)\}_{t=1}^T$ were post-processed to identify characteristic operating points based on the desired velocity. The resulting measurements constitute the ground-truth dataset for training and validating the PIK model. This selection strategy ensures the surrogate captures nonlinear effects such as saturation and friction across the full actuator envelope.

Notation 1: Let (τ_e, ω_m) denote the PMSM's torque and angular velocity, and let $[F_{L,\text{phys}}, \dot{x}_{L,\text{phys}}, \eta_{\text{phys}}, i_{abc,\text{phys}}]$ denote the corresponding analytic outputs. The analytic model

M2L, derived from Section II, maps the motor-side outputs to EMLA's load-side features:

$$(F_{L,\text{phys}}, \dot{x}_{L,\text{phys}}, \eta_{\text{phys}}, i_{abc,\text{phys}}) = \text{M2L}(\tau_e, \omega_m). \quad (24)$$

This model serves as the physics-informed mean function around which the Gaussian-process residuals are learned.

B. Physics-Informed GP Training and Evaluation

For each training sample (τ_e^k, ω_m^k) , we compute the analytic outputs via M2L and define the residuals as

$$\begin{cases} \mathcal{R}_{F_L}^k = \tilde{F}_L^k - F_{L,\text{phys}}^k, \\ \mathcal{R}_{\dot{x}_L}^k = \tilde{\dot{x}}_L^k - \dot{x}_{L,\text{phys}}^k, \\ \mathcal{R}_\eta^k = \tilde{\eta}^k - \eta_{\text{phys}}^k, \\ \mathcal{R}_{i_{abc}}^k = \tilde{i}_{abc}^k - i_{abc,\text{phys}}^k. \end{cases} \quad (25)$$

We then assemble the raw feature matrix of motor-side variables,

$$X_{\text{raw}} \triangleq \begin{bmatrix} \tau_e^1 & \omega_m^1 \\ \tau_e^2 & \omega_m^2 \\ \vdots & \vdots \\ \tau_e^N & \omega_m^N \end{bmatrix} \in \mathbb{R}^{N \times 2}, \quad (26)$$

and compute column-wise means and standard deviations

$$\begin{cases} \mu_j = \frac{1}{N} \sum_{k=1}^N X_{\text{raw},j}^k, \\ \sigma_j = \sqrt{\frac{1}{N-1} \sum_{k=1}^N (X_{\text{raw},j}^k - \mu_j)^2}, \end{cases} \quad j = 1, 2, \quad (27)$$

to normalize each input feature as

$$X_{n,j}^k = \frac{X_{\text{raw},j}^k - \mu_j}{\sigma_j}, \quad k = 1, \dots, N, \quad j = 1, 2. \quad (28)$$

The vectors $\mu, \sigma \in \mathbb{R}^2$ are stored to ensure identical preprocessing during prediction with the PIK model.

Four independent Gaussian-process models, one for each output $q \in \{F_L, \dot{x}_L, \eta, i_{abc}\}$, are trained with an ARD squared-exponential kernel. The analytic map M2L serves as the mean function, while hyperparameters are tuned via quasi-Newton optimization, as summarized in Algorithm 3.

After fitting, the collection of GPs and normalization parameters is saved as $\text{gpPIK} = \{\mathcal{G}_{F_L}, \mathcal{G}_{\dot{x}_L}, \mathcal{G}_\eta, \mathcal{G}_{i_{abc}}, \mu, \sigma\}$. Kernel length-scales and noise variances are tuned via quasi-Newton maximization of the log-marginal likelihood (initialized using the data's standard deviations). This PIK training scheme learns only the discrepancies between measured outputs and the inexpensive analytic map M2L, yielding accurate, sub-millisecond predictions suitable for real-time control.

Given P new motor-side pairs $\{(\tau_e^p, \omega_m^p)\}_{p=1}^P$, the PIK surrogate computes load-side predictions and uncertainties as detailed in Algorithm 4.

We assess the surrogate's predictive accuracy both qualitatively, through residual maps with uncertainty bands, and quantitatively, via RMSE on a hold-out test set. For each test sample $p = 1, \dots, P$, the surrogate outputs $\{F_{L,\text{pred}}, \dot{x}_{L,\text{pred}}, \eta_{\text{pred}}, i_{abc,\text{pred}}\}$ with predictive standard

Algorithm 3 PIK Surrogate Training for the EMLA

Require: $\{\tilde{F}_L(t), \tilde{x}_L(t), \tilde{\eta}(t), \tilde{\tau}_e(t), \tilde{\omega}_m(t), \tilde{i}_{abc}(t)\}_{t=1}^T$
Ensure: Trained model gpPIKModel

```

1: for  $k = 1, \dots, N$  do
2:   Extract  $(\tilde{F}_L^k, \tilde{x}_L^k, \tilde{\tau}_e^k, \tilde{\omega}_m^k, \tilde{\eta}^k, \tilde{i}_{abc}^k)$ 
3:    $(F_{L,\text{phys}}^k, \dot{x}_{L,\text{phys}}^k, \eta_{\text{phys}}^k, i_{abc,\text{phys}}^k) \leftarrow \text{M2L}(\tau_e^k, \omega_m^k)$ 
4: end for
5:  $\mathcal{R}_q^k = \tilde{q}^k - q_{\text{phys}}^k$  for each  $q \in \{F_L, \dot{x}_L, \eta, i_{abc}\}$ 
6:  $X_{\text{raw}}[k, :] \leftarrow [\tau_e^k, \omega_m^k] \in \mathbb{R}^{N \times 2}$ 
7:  $\mu_j \leftarrow \frac{1}{N} \sum_{k=1}^N X_{\text{raw}}[k, j]$ 
8:  $\sigma_j \leftarrow \sqrt{\frac{1}{N-1} \sum_{k=1}^N (X_{\text{raw}}[k, j] - \mu_j)^2}$ 
9:  $X_{\text{norm}}[k, j] \leftarrow (X_{\text{raw}}[k, j] - \mu_j) / \sigma_j$ 
10:  $m(X) \leftarrow \text{M2L}(X[:, 1] \cdot \sigma_1 + \mu_1, X[:, 2] \cdot \sigma_2 + \mu_2)$ 
11: for  $q \in \{F_L, \dot{x}_L, \eta, i_{abc}\}$  do
12:    $\mathcal{G}_q \leftarrow \text{fitrgp}(X_{\text{norm}}, \mathcal{R}_q, m)$ 
13: end for
14: gpPIKModel  $\leftarrow \{\mathcal{G}_{F_L}, \mathcal{G}_{\dot{x}_L}, \mathcal{G}_{\eta}, \mathcal{G}_{i_{abc}}, \mu, \sigma\}$ 
15: save('gpPIKModel.mat', 'gpPIKModel')
16: return gpPIKModel

```

Algorithm 4 PIK Surrogate Prediction

Require: Motor-side inputs $\{(\tau_e^p, \omega_m^p)\}_{p=1}^P$, trained model gpPIK = $\{\mathcal{G}_q, \mu \in \mathbb{R}^2, \sigma \in \mathbb{R}^2\}$
Ensure: Output predictions $Y_{\text{pred}} \in \mathbb{R}^{P \times 4}$

```

1: for  $p = 1, \dots, P$  do
2:    $X_{\text{raw}}[p, :] \leftarrow [\tau_e^p, \omega_m^p]$ 
3:   for  $j = 1, 2$  do
4:      $X_n[p, j] \leftarrow \frac{X_{\text{raw}}[p, j] - \mu_j}{\sigma_j}$ 
5:   end for
6: end for
7:  $B_{\text{phys}} \leftarrow \text{M2L}(X_{\text{raw}})$ 
8: for  $q = 1$  to 4 do
9:    $(r_q, s_q) \leftarrow \text{predict}(\mathcal{G}_q, X_n)$ 
10:   $\Sigma(:, q) \leftarrow s_q$ 
11:   $Y_{\text{pred}}(:, q) \leftarrow B_{\text{phys}}(:, q) + r_q$ 
12: end for
13: return  $Y_{\text{pred}}$ 

```

deviations $\{\sigma_{F_L}, \sigma_{\dot{x}_L}, \sigma_{\eta}, \sigma_{i_{abc}}\}$. Using measured values \tilde{q}^p , we define the signed absolute error $e_q^p = \tilde{q}^p - q_{\text{pred}}^p$ and the signed percentage residual

$$r_q^p = 100 \times \frac{\tilde{q}^p - q_{\text{pred}}^p}{\tilde{q}^p}, \quad q \in \{F_L, \dot{x}_L, \eta, i_{abc}\}. \quad (29)$$

Residual maps with $\pm 2\sigma$ uncertainty bands are shown in Fig. 5, indicating that errors remain within the predicted bounds and that uncertainty increases smoothly in sparse data regions. On the hold-out test set, the surrogate achieves $\text{RMSE}_{F_L} = 0.127$ kN, $\text{RMSE}_{\dot{x}_L} = 0.001$ m/s, $\text{RMSE}_{\eta} = 0.23\%$, and $\text{RMSE}_{i_{abc}} = 0.0035$ A. Measured versus predicted values are plotted in Fig. 6, showing close alignment across all outputs.

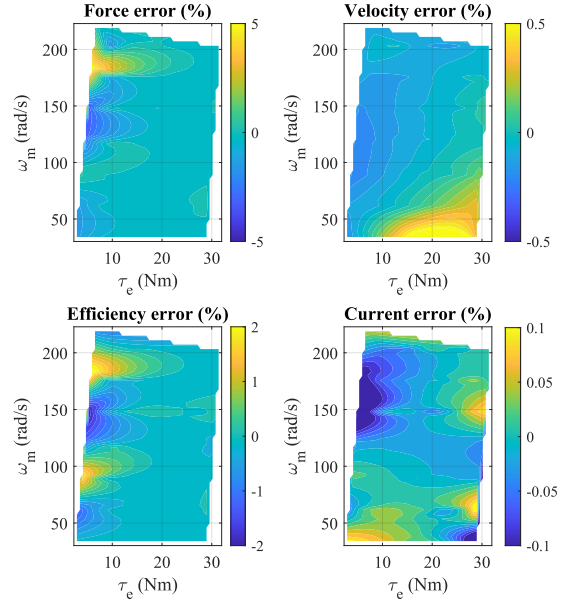


Fig. 5. Residuals with predictive uncertainty ($\pm 2\sigma$) across the torque-speed domain, confirming calibrated confidence intervals.

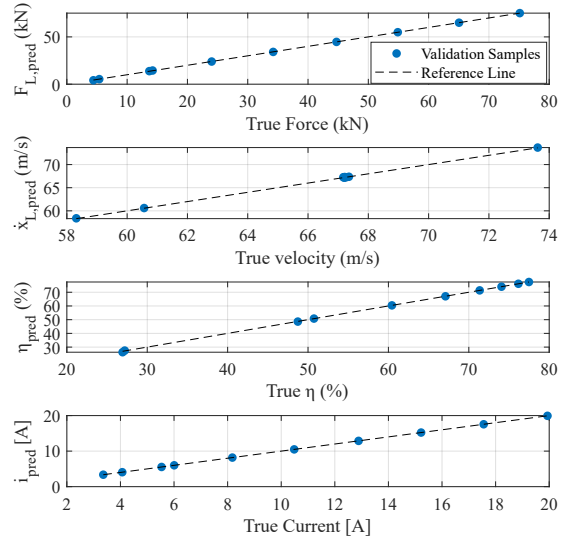


Fig. 6. True versus predicted on the hold-out test set for force, velocity, efficiency, and current.

VI. CONTROLLER DESIGN

In this section, the performance of the optimized EMLA configuration obtained in Section IV is evaluated to verify its capability to meet the required speed and force demands. Consequently, a controller must be designed for this system.

Building on the physics-informed Kriging (PIK) surrogate of the EMLA developed in Section V, a hierarchical control framework is employed, as illustrated in Fig. 7. At the high level, the VDC controller determines the required velocities and forces for each actuator, while at the low level, a dedicated controller generates the control voltages needed to achieve the commanded speed and force.

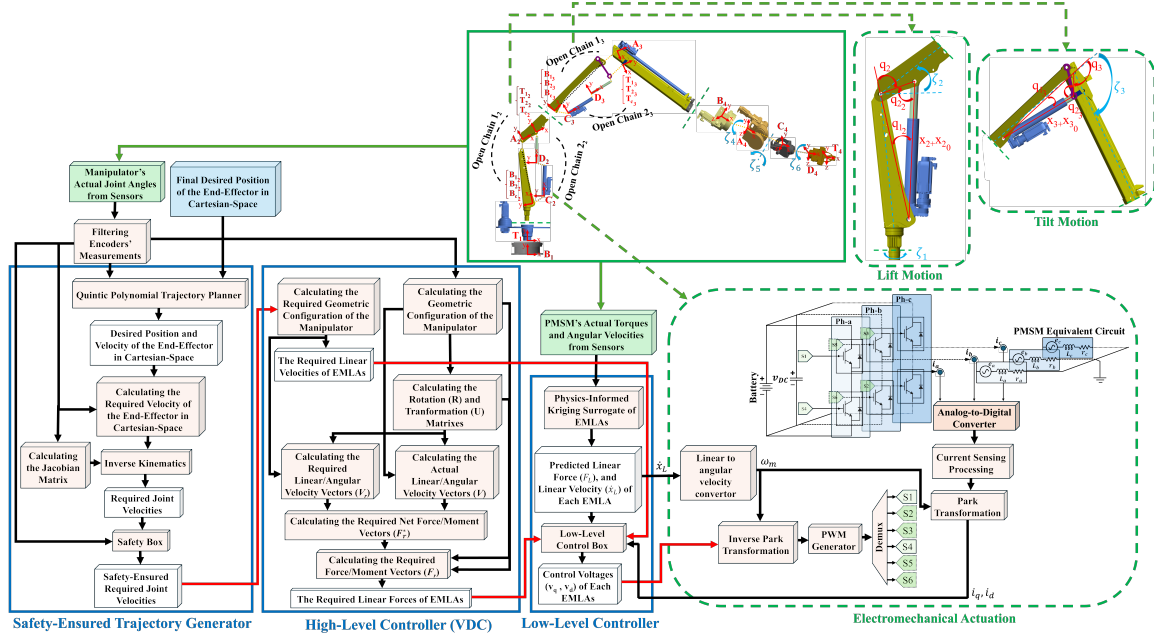


Fig. 7. Schematic of the Motion Planning and Control of the HDRM

A. High-Level Control

Remark 4: The high-level controller used here was introduced in [23] with full details; therefore, only a brief summary is provided.

As shown in Fig. 7, a modular adaptive VDC controller serves as the high-level controller. It computes the required linear velocities and forces for the EMLAs using safety-ensured joint velocity commands from the trajectory generator and filtered joint angle measurements.

Following the VDC framework [27] and the procedure in [23], the robot's actual and required geometric configurations are determined from the filtered joint angles and the required joint velocities. Subsequently, the required linear velocities of all EMLAs (\dot{x}_{L_r}) are obtained, and the associated rotation and transformation matrices are calculated using (8).

Finally, the actual and required linear/angular velocity vectors expressed in any frame $\{A\}$, denoted by ${}^A V$, ${}^A V_r \in \mathbb{R}^6$, are computed recursively from the base to the end-effector using Algorithm 5, as illustrated in Fig. 7.

Once the actual and required linear/angular velocity vectors are obtained, the required net force/moment vector in frame $\{A\}$, denoted ${}^A F_r^* \in \mathbb{R}^6$, is computed as:

$${}^A F_r^* = Y_A \hat{\theta}_A + K_A ({}^A V_r - {}^A V), \quad (30)$$

where $K_A \in \mathbb{R}^{6 \times 6}$ is a positive-definite gain matrix, $Y_A({}^A \dot{V}_r, {}^A V_r) \in \mathbb{R}^{6 \times 10}$ is the regressor matrix, and $\hat{\theta}_A$ provides an estimate of the inertial parameter vector θ_A via the natural adaptation law [23].

Following the VDC framework, the required force/moment vector in any frame $\{A\}$, ${}^A F_r \in \mathbb{R}^6$, is then computed recursively from the end-effector to the base using Algorithm 6.

The required linear force for each EMLA (F_{L_r}) is subsequently determined from these results.

Algorithm 5 Systematic VDC-Based Kinematics

Require: VDC model structure, joint variables (ζ_j)

Ensure: Linear/angular velocity vectors for all components

```

1: if  $j = 1$  (base motion) then
2:   Compute:  $\begin{cases} T_j V = y_r \dot{\zeta}_j + B_j U_{T_j}^T B_j V \\ B_{c_{j+1}} V = T_j U_{B_{c_{j+1}}}^T T_j V \end{cases}$ 
3: else if  $j = 2$  (lift motion) or  $j = 3$  (tilt motion) then
4:   for  $j = 2$  to 3 do
5:     Chain 1j:  $\begin{cases} A_j V = z_r \dot{q}_j + B_{1j} U_{A_j}^T B_{1j} V \\ T_{1j} V = A_j U_{T_{1j}}^T A_j V \end{cases}$ 
6:     Chain 2j:  $\begin{cases} C_j V = z_r \dot{q}_{1j} + B_{2j} U_{C_j}^T B_{2j} V \\ D_j V = x_f \dot{x}_j + C_j U_{D_j}^T C_j V \\ T_{2j} V = z_r \dot{q}_{2j} + D_j U_{T_{2j}}^T D_j V \end{cases}$ 
7:     Motion constraints:  $\begin{cases} B_{1j} V = B_{2j} V = B_{c_j} V \\ T_{1j} V = T_{2j} V = T_{c_j} V \end{cases}$ 
8:     Propagate:  $B_{c_{j+1}} V = T_{c_j} U_{B_{c_{j+1}}}^T T_{c_j} V$ 
9:   end for
10: else if  $j = 4$  (wrist motion) then
11:   Compute:  $\begin{cases} A_j V = x_r \dot{\zeta}_j + B_j U_{A_j}^T B_j V \\ C_j V = z_r \dot{\zeta}_{j+1} + A_j U_{C_j}^T A_j V \\ D_j V = x_r \dot{\zeta}_{j+2} + C_j U_{D_j}^T C_j V \\ T_j V = D_j U_{T_j}^T D_j V \end{cases}$ 
12: end if

```

B. Low-Level Control

Remark 5: The low-level controller was originally introduced in [23]. To address practical constraints and reduce sensor costs, it was redesigned to operate without force and velocity sensors by leveraging the PIK surrogate from

Algorithm 6 Systematic VDC-Based Dynamics

Require: VDC model structure, required net force/moment vectors (\mathbf{F}_r^*)

Ensure: Required Force/moment vectors for all components

```

1: if  $j = 4$  (wrist motion) then
2:   Compute:  $\begin{cases} \mathbf{D}_j \mathbf{F}_r = \mathbf{D}_j \mathbf{F}_r^* + \mathbf{D}_j \mathbf{U}_{T_j} \mathbf{T}_j \mathbf{F}_r \\ \mathbf{C}_j \mathbf{F}_r = \mathbf{C}_j \mathbf{F}_r^* + \mathbf{C}_j \mathbf{U}_{D_j} \mathbf{D}_j \mathbf{F}_r \\ \mathbf{A}_j \mathbf{F}_r = \mathbf{A}_j \mathbf{F}_r^* + \mathbf{A}_j \mathbf{U}_{C_j} \mathbf{C}_j \mathbf{F}_r \\ \mathbf{B}_j \mathbf{F}_r = \mathbf{B}_j \mathbf{F}_r^* + \mathbf{B}_j \mathbf{U}_{A_j} \mathbf{A}_j \mathbf{F}_r \end{cases}$ 
3: else if  $j = 3$  (tilt motion) or  $j = 2$  (lift motion) then
4:   for  $j = 3$  to 2 do
5:     Compute:

$$\mathbf{B}_{c_j} \mathbf{F}_r = \mathbf{B}_{1j} \mathbf{F}_r^* + \mathbf{B}_{1j} \mathbf{U}_{A_j} \mathbf{A}_j \mathbf{F}_r^* + \mathbf{B}_{2j} \mathbf{U}_{C_j} \mathbf{C}_j \mathbf{F}_r^* + \mathbf{B}_{2j} \mathbf{U}_{C_j} \mathbf{C}_j \mathbf{U}_{D_j} \mathbf{D}_j \mathbf{F}_r^* + \mathbf{B}_{1j} \mathbf{U}_{A_j} \mathbf{A}_j \mathbf{U}_{B_{j+1}} \mathbf{B}_{j+1} \mathbf{F}_r$$

6:   end for
7: else if  $j = 1$  (base motion) then
8:   Compute:  $\mathbf{T}_j \mathbf{F}_r = \mathbf{T}_j \mathbf{F}_r^* + \mathbf{T}_j \mathbf{U}_{B_{c_{j+1}}} \mathbf{B}_{c_{j+1}} \mathbf{F}_r$ 
9: end if

```

Section V.

The required velocity and force from Section VI-A are tracked by each EMLA, as illustrated in Fig. 7. First, based on the measured PMSM torque and angular velocity, the predicted load-side force $F_{L,\text{pred}} = Y_{\text{pred}}(:, 1)$ and predicted linear velocity $\dot{x}_{L,\text{pred}} = Y_{\text{pred}}(:, 2)$ are obtained using the surrogate PIK model (Algorithm 4). The required voltage inputs for the EMLA are then computed as [23]:

$$\begin{cases} v_{d_r} = r_s i_d + L_d \frac{di_{d_r}}{dt} - L_q P \omega_m i_q + K_i (i_{d_r} - i_d), \\ v_{q_r} = r_s i_q + L_q \frac{di_{q_r}}{dt} + L_d P \omega_m i_d + P \psi_f \omega_m \\ \quad + K_f (F_{L_r} - F_{L,\text{pred}}) + K_v (\dot{x}_{L_r} - \dot{x}_{L,\text{pred}}). \end{cases} \quad (31)$$

Here, K_i , K_f , and K_v are positive scalar gains for current, force, and velocity tracking; i_d and i_q are the PMSM currents; and F_{L_r} and \dot{x}_{L_r} are the high-level controller's required values. The feedforward terms account for electromechanical dynamics, while the feedback terms improve tracking accuracy and stability. The full hierarchical control, integrating the high-level VDC and low-level actuator controllers, is presented in Algorithm 7.

Remark 6: The stability of the proposed modular control is analyzed in Section IV.C of [23] using Lyapunov theory, and its robustness to parametric uncertainties is discussed in Section V.A.

VII. EXPERIMENTAL RESULTS

This section aims to: (i) assess the optimized EMLA configuration in meeting speed and force requirements, (ii) validate the safety-ensured (SE) trajectory generator, and (iii) compare the proposed sensorless (SL) VDC with the measurement-feedback (MF) VDC. To achieve these objectives, trajectories are designed to demand maximum velocity and reach joint limits, with payloads ranging from 0 to 300 kg. Fig. 8 shows

Algorithm 7 PIK-Enhanced VDC for All-Electric HDRM

Require: Required joint velocities ($\dot{\zeta}_{r_j}$), joint angle measurements (ζ_j), and PMSMs' torques and angular velocities (τ_{e_j}, ω_{m_j})

Ensure: Voltage commands for actuators $\{v_{q_j}, v_{d_j}\}_{j=1}^6$

Initialization:

Load each joint's PIK surrogate `gpPIKModelj`

```

1: while control active do
2:   for  $j = 1$  to 6 do
3:     High-Level Control:
4:     Read joint states  $\zeta_j, \dot{\zeta}_j$ 
5:     Compute  $\mathbf{V}$  using  $\dot{\zeta}_j$  (Algorithm 5)
6:     Compute  $\mathbf{V}_r$  using  $\zeta_{r_j}$  (Algorithm 5)
7:     Compute the required linear velocities of EMLAs
8:     Compute  $\mathbf{A} \mathbf{F}_r^* = \mathbf{Y}_A \hat{\theta}_A + \mathbf{K}_A (\mathbf{A} \mathbf{V}_r - \mathbf{A} \mathbf{V})$ 
9:     Compute  $\mathbf{F}_r$  (Algorithm 6)
10:    Compute the required linear forces of EMLAs
11:    Low-Level Control:
12:     $Y_{\text{pred}}(j, :) = \text{PredPIK}(\tau_{e_j}, \omega_{m_j})$ 
13:     $\{F_{L,\text{pred}}, \dot{x}_{L,\text{pred}}\} \leftarrow Y_{\text{pred}}(j, :)$ 
14:    Compute  $v_{q_r}$  and  $v_{d_r}$  for each EMLA from (31)
15:    Send  $v_{q_r}$  and  $v_{d_r}$  via EtherCAT
16:   end for
17: end while

```

the required position and velocity before and after applying the safety constraints, as introduced in Section III-B.

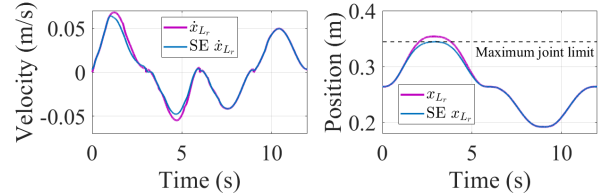


Fig. 8. Required position and velocity, in the joint-space, before and after applying safety constraints.

The results indicate that the SE trajectory effectively constrains joint motion within the safe range, ensuring that the maximum joint limit is not exceeded. Fig. 9 presents the required and emulated linear forces for SE trajectory tracking with payloads ranging from 0 to 300 kg. Subsequently, using the SE trajectory generator, Figs. 10–13 compare the position and velocity profiles of the VDC-SL and VDC-MF controllers.

It is observed that the VDC-SL accurately tracked position, velocity, and force, demonstrating robustness without linear velocity and force measurements. A quantitative comparison between the VDC-SL and VDC-MF is presented in Table I, using root mean square (RMS) and maximum (Max) tracking errors for position and velocity.

Table I indicates that both controllers exhibit increasing errors with larger payloads, highlighting the influence of HDRM inertia. The sensorless controller (VDC-SL) shows slightly higher RMS and maximum errors compared to the measurement-feedback controller (VDC-MF); however, all

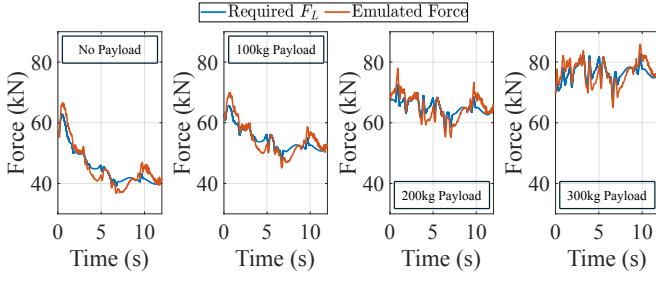


Fig. 9. Comparison of the required force F_{Lr} and the emulated force for different payloads.

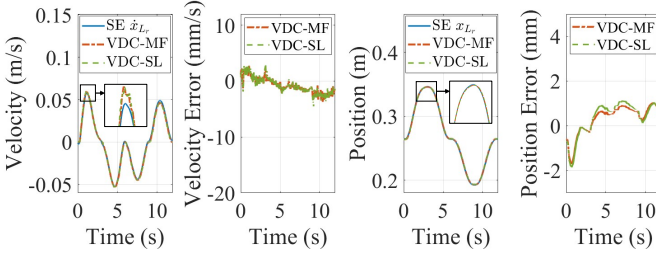


Fig. 10. Tracking performance and errors under no payload condition.

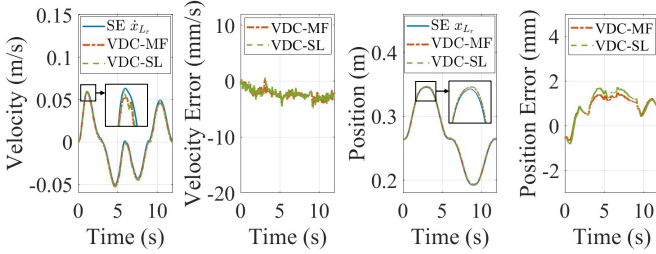


Fig. 11. Tracking performance and errors under a 100 kg payload.

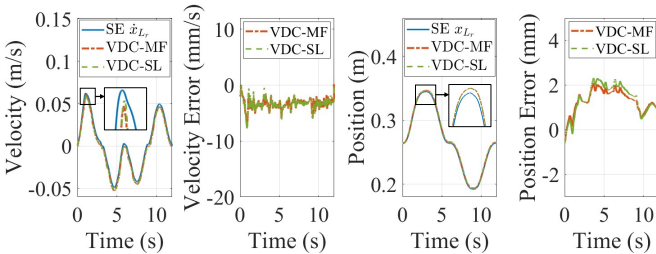


Fig. 12. Tracking performance and errors under a 200 kg payload.

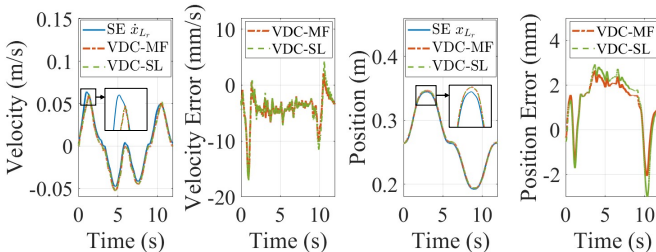


Fig. 13. Tracking performance and errors under a 300 kg payload.

TABLE I
TRACKING ERRORS OF VDC-MF AND VDC-SL UNDER DIFFERENT PAYLOAD CONDITIONS

Payload	Metric	VDC-MF Errors		VDC-SL Errors	
		Position	Velocity	Position	Velocity
0 kg	RMS	0.72	1.56	0.82	1.63
	Max	1.71	3.71	1.86	4.50
100 kg	RMS	1.03	2.39	1.16	2.41
	Max	1.49	4.57	1.73	4.88
200 kg	RMS	1.39	3.45	1.52	3.48
	Max	2.10	7.19	2.32	7.86
300 kg	RMS	1.66	4.97	1.89	5.14
	Max	2.65	16.74	3.01	17.03

- Position errors are expressed in millimeters (mm).

- Velocity errors are expressed in millimeters per second (mm/s).

errors remain within acceptable limits, confirming accurate position, velocity, and force tracking. Notably, the sharp rise in maximum velocity error at 300 kg reflects the effects of inertia and actuator power saturation, whereas the moderate increase in RMS errors indicates stable overall performance across the payload range.

VIII. CONCLUSION

This paper presented a comprehensive framework for electrifying and achieving sensorless control of HDRMs using EMLAs. An integrated EMLA model combining PMSM electromechanics and directional screw-thread efficiency was embedded within a VDC-based joint-space architecture. Actuator sizing was formulated as a multi-objective NSGA-II problem over motor choice, gearbox ratio, and screw lead, accelerated via a deep neural-network model for sub-millisecond actuator efficiency predictions. For sensorless control, a physics-informed Kriging surrogate reconstructed load-side force, velocity, and three-phase currents from only torque and angular velocity measurements. Integration of this surrogate into the VDC controller was experimentally validated on a one-degree-of-freedom testbed, demonstrating accurate trajectory tracking under varying loads. The results confirm that the Kriging observer eliminates the need for dedicated force and velocity sensors, while the VDC control ensures precise performance across a wide operating range. By uniting detailed modeling, multi-objective design, and sensorless control, this work lays the foundation for replacing hydraulic actuation with efficient, zero-emission EMLAs in HDRMs.

REFERENCES

- [1] United Nations Framework Convention on Climate Change, "The paris agreement," 2015, accessed: 2025-08-11. [Online]. Available: <https://unfccc.int/process-and-meetings/the-paris-agreement/the-paris-agreement>
- [2] European Parliament and Council, "Regulation (eu) 2023/851 of the european parliament and of the council of 19 april 2023 amending regulation (eu) 2019/631," *Official Journal of the European Union*, no. L 110, pp. 5–20, Apr. 2023. [Online]. Available: <https://eur-lex.europa.eu/eli/reg/2023/851/oj/eng>
- [3] P. Sorknæs, R. M. Johannsen, A. D. Korberg, T. B. Nielsen, U. R. Petersen, and B. V. Mathiesen, "Electrification of the industrial sector in 100% renewable energy scenarios," *Energy*, vol. 254, p. 124339, 2022.

- [4] S. Bellocchi, M. Manno, M. Noussan, M. G. Prina, and M. Vellini, "Electrification of transport and residential heating sectors in support of renewable penetration: Scenarios for the Italian energy system," *Energy*, vol. 196, p. 117062, 2020.
- [5] J. Mattila, J. Koivumäki, D. G. Caldwell, and C. Semini, "A survey on control of hydraulic robotic manipulators with projection to future trends," *IEEE/ASME Transactions on Mechatronics*, vol. 22, no. 2, pp. 669–680, 2017.
- [6] N. D. Manring, "Efficiency mapping for a linear hydraulic-actuator," *Journal of Dynamic Systems, Measurement, and Control*, vol. 135, no. 6, p. 064505, 2013.
- [7] J. B. Chipka, M. A. Meller, and E. Garcia, "Efficiency testing of hydraulic artificial muscles with variable recruitment using a linear dynamometer," in *Bioinspiration, Biomimetics, and Bioreplication 2015*, vol. 9429. SPIE, 2015, pp. 193–202.
- [8] J. Pustavrh, M. Hočevr, P. Podržaj, A. Trajkovski, and F. Majdič, "Comparison of hydraulic, pneumatic and electric linear actuation systems," *Scientific Reports*, vol. 13, no. 1, p. 20938, 2023.
- [9] R. Stokke, X. Qiu, M. Sparrevik, S. Truloff, I. Borge, and L. De Boer, "Procurement for zero-emission construction sites: a comparative study of four European cities," *Environment Systems and Decisions*, vol. 43, no. 1, pp. 72–86, 2023.
- [10] M. Bahari, A. Paz, M. H. Shahna, P. Mustalahti, and J. Mattila, "System-level efficient performance of emla-driven heavy-duty manipulators via bilevel optimization framework with a leader-follower scenario," *IEEE Transactions on Automation Science and Engineering*, 2025.
- [11] S. Qu, F. Zappaterra, A. Vacca, and E. Busquets, "An electrified boom actuation system with energy regeneration capability driven by a novel electro-hydraulic unit," *Energy Conversion and Management*, vol. 293, p. 117443, 2023.
- [12] F. Tootoonchian and Z. Nasiri-Gheidari, "Cogging force mitigation techniques in a modular linear permanent magnet motor," *IET Electric Power Applications*, vol. 10, no. 7, pp. 667–674, 2016.
- [13] H. Saneie, Z. Nasiri-Gheidari, and F. Tootoonchian, "Design and prototyping of a multi-turn sinusoidal air-gap length resolver," *IEEE Transactions on Energy Conversion*, vol. 35, no. 1, pp. 271–278, 2020.
- [14] M. Khajeezadeh, F. Zare, and Z. Nasiri-Gheidari, "Reliability analysis of two resolver configurations under faulty conditions in 2dof system," *IEEE Transactions on Instrumentation and Measurement*, vol. 72, pp. 1–8, 2022.
- [15] L. Li, L. Xie, X. Luo, and Z. Wang, "Compliance control using hydraulic heavy-duty manipulator," *IEEE Transactions on Industrial Informatics*, vol. 15, no. 2, pp. 1193–1201, 2018.
- [16] T. Mononen, M. M. Aref, and J. Mattila, "Nonlinear model predictive control of a heavy-duty hydraulic bulldozer blade," in *2019 IEEE International Conference on Cybernetics and Intelligent Systems (CIS) and IEEE Conference on Robotics, Automation and Mechatronics (RAM)*. IEEE, 2019, pp. 565–570.
- [17] Z. Yao, F. Xu, G.-P. Jiang, and J. Yao, "Data-driven control of hydraulic manipulators by reinforcement learning," *IEEE/ASME Transactions on Mechatronics*, vol. 29, no. 4, pp. 2673–2684, 2023.
- [18] X. Liang, Z. Yao, W. Deng, and J. Yao, "Adaptive neural network finite-time tracking control for uncertain hydraulic manipulators," *IEEE/ASME Transactions on Mechatronics*, vol. 30, no. 1, pp. 645–656, 2024.
- [19] H. V. A. Truong, S. Nam, S. Kim, Y. Kim, and W. K. Chung, "Backstepping-sliding-mode-based neural network control for electro-hydraulic actuator subject to completely unknown system dynamics," *IEEE Transactions on Automation Science and Engineering*, vol. 21, no. 4, pp. 6202–6216, 2023.
- [20] M. Hejrati and J. Mattila, "Orchestrated robust controller for precision control of heavy-duty hydraulic manipulators," *IEEE Transactions on Automation Science and Engineering*, 2025.
- [21] N. T. Dat, C. Van Kien, and H. P. H. Anh, "Advanced adaptive neural sliding mode control applied in pmsm driving system," *Electrical Engineering*, vol. 105, no. 5, pp. 3255–3262, 2023.
- [22] S. Niu, Y. Luo, W. Fu, and X. Zhang, "Robust model predictive control for a three-phase pmsm motor with improved control precision," *IEEE Transactions on Industrial Electronics*, vol. 68, no. 1, pp. 838–849, 2020.
- [23] A. H. Barjini, M. Bahari, M. Hejrati, and J. Mattila, "Surrogate-enhanced modeling and adaptive modular control of all-electric heavy-duty robotic manipulators," *arXiv preprint arXiv:2508.06313*, 2025.
- [24] S. Singh and A. Tiwari, "Various techniques of sensorless speed control of pmsm: A review," in *2017 Second International Conference on Electrical, Computer and Communication Technologies (ICECCT)*. IEEE, 2017, pp. 1–6.
- [25] A. A. Abbas, J. Vesa, H. Khan, H. Chen, Y. Liu, and P. Rasilo, "Fast and accurate non-linear model for synchronous machines including core losses," *IEEE Transactions on Energy Conversion*, vol. 39, no. 4, pp. 2559–2567, 2024.
- [26] M. Heydari Shahna, M. Bahari, and J. Mattila, "Robustness-guaranteed observer-based control strategy with modularity for cleantech emla-driven heavy-duty robotic manipulator," *IEEE Transactions on Automation Science and Engineering*, vol. 22, pp. 10 248–10 273, 2025.
- [27] W.-H. Zhu, *Virtual decomposition control: toward hyper degrees of freedom robots*. Springer Science & Business Media, 2010, vol. 60.
- [28] M. Hejrati and J. Mattila, "Decentralized nonlinear control of redundant upper limb exoskeleton with natural adaptation law," in *2022 IEEE-RAS 21st International Conference on Humanoid Robots (Humanoids)*. IEEE, 2022, pp. 269–276.
- [29] K. Deb, A. Pratap, S. Agarwal, and T. Meyarivan, "A fast and elitist multiobjective genetic algorithm: Nsga-ii," *IEEE transactions on evolutionary computation*, vol. 6, no. 2, pp. 182–197, 2002.



Mohammad Bahari earned a B.Sc. in electrical engineering power from Semnan University, Semnan, Iran, in 2015, followed by the completion of his M.Sc. in electrical engineering power electronics and electric machines from Sharif University of Technology, Tehran, Iran, in 2019. Presently, he is engaged as a doctoral researcher at Tampere University, Tampere, Finland, focusing on design and control of an all-electric robotic e-boom. His research interests include multidisciplinary design optimization of electromechanical actuator.



Amir Hossein Barjini received a B.Sc. in Mechanical Engineering from Amirkabir University of Technology (AUT), Tehran, Iran, in 2021, and an M.Sc. in Mechanical Engineering from Sharif University of Technology (SUT), Tehran, Iran, in 2024. Currently, he is a doctoral researcher at Tampere University, Tampere, Finland. His research interests include applications of artificial intelligence in control, automation, and robotics.



Pauli Mustalahti received his M.Sc. degree in engineering from the Tampere University of Technology in 2016 and his D.Sc. (Tech.) degree in Automation Science and Engineering from Tampere University in 2023. He is a researcher in the Unit of Automation Technology and Mechanical Engineering, Tampere University, Tampere, Finland. His research interests include nonlinear model-based control of robotic manipulators.



Jouni Mattila received an M.Sc. and Ph.D. in automation engineering from Tampere University of Technology, Tampere, Finland, in 1995 and 2000, respectively. He is currently a professor of machine automation with the Unit of Automation Technology and Mechanical Engineering at Tampere University. His research interests include machine automation, nonlinear-model-based control of robotic manipulators, and energy-efficient control of heavy-duty mobile manipulators.